

**Concentration-Dependent Tungsten Effects on Short-Range Order and Deformation
Behavior in Ni–W alloys**

Shaozun Liu^{1,7*}, Zehao Li², Hantong Chen³, Xingyuan San⁴, Bi-Cheng Zhou^{3*}, Dieter Isheim^{2,8},
Tiejun Wang¹, Hong Gao⁵, Nie Zhao⁶, Yu Liu¹, Yong Gan¹, Xiaobing Hu^{2,9*}

¹Central Iron and Steel Research Institute, Beijing 100081, China

²Department of Materials Science and Engineering, Northwestern University, Evanston, IL 60208,
USA

³Department of Materials Science and Engineering, University of Virginia, Charlottesville,
Virginia 22904, USA

⁴Hebei Key Lab of Optic-electronic Information and Materials, The College of Physics Science
and Technology, Hebei University, Baoding 071002, China

⁵Department of Physics, Beihang University, Beijing 100191, China

⁶School of Materials Science and Engineering, Xiangtan University, Xiangtan 411105, China

⁷Yangjiang Advanced Alloys Laboratory, Yangjiang 529500, China

⁸Northwestern University Center for Atom Probe Tomography (NUCAPT), Evanston, IL 60208,
USA

⁹The NUANCE Center, Northwestern University, Evanston, IL 60208, USA

*Corresponding authors. Email: xbhu@northwestern.edu (X.H.); liushaozun@cisri.com (S.L.);
bicheng.zhou@virginia.edu (B.C.Z.);

Abstract

Ni–W based medium heavy alloys offer a promising pathway to bridge the density–strength gap between tungsten heavy alloys and ultrahigh-strength steels. In this study, the effects of W concentration on short-range order (SRO), deformation behavior, and grain boundary chemistry of Ni– x W in the range of $x=0$ to 38 wt.% alloys were systematically investigated using a suite of advanced characterization and modeling techniques, including synchrotron X-ray diffraction, transmission electron microscopy, atom probe tomography, and first-principles thermodynamic simulations. Our study reveals that strong SRO emerges when W content exceeds ~30 wt.%, producing distinct diffuse scattering and significantly enhancing strain-hardening capacity. During deformation, the presence of SRO promotes planar slip and twin formation, leading to strong dislocation interactions and elevated flow stress. Hall–Petch analysis demonstrates an exceptionally high grain boundary strengthening coefficient ($k_y \approx 1102 \text{ MPa}\cdot\mu\text{m}^{-1/2}$) in Ni–38W, underscoring the intrinsic strengthening effect associated with SRO. First-principles cluster expansion coupled with Monte Carlo simulations reveals that increasing W content enhances SRO tendency through the stabilization of Ni₄W type local configurations. These findings establish a mechanistic link between W concentration, SRO evolution, and mechanical response, providing new insights for designing high-density, high-strength Ni–W based alloys with optimized performance.

Key words: Medium heavy alloys, short-range order, solid solution strengthening, plane glide, deformation twin

1. Introduction

Tungsten heavy alloys (WHAs) have long been recognized as indispensable structural and functional materials due to their high density, balanced strength and toughness, excellent electrical and thermal conductivity, and superior resistance to wear, corrosion, and oxidation [1-6]. These properties make WHAs vital in a wide range of applications, spanning from defense and aerospace to medical and nuclear industries. Their combination of mass and durability enables their use in armor-piercing projectiles, counterweights for missiles and aircraft, radiation shielding, and advanced electrical and mechanical tooling. Despite these advantages, the broad application of WHAs has been constrained by their limited mechanical performance, especially when benchmarked against ultrahigh strength steels (UHSSs) [7-13]. The root of this limitation lies in the intrinsic characteristics of the body-centered cubic (BCC) tungsten (W) matrix, which suffers from poor ductility and a restricted ability to accommodate plastic deformation. Consequently, while WHAs provide density advantages, they fall short in mechanical robustness compared with steel-based systems. By contrast, UHSSs exhibit exceptional strength and toughness, making them attractive for structural applications in automotive, aerospace, and energy sectors. However, their low density ($\sim 7.8\text{--}8.1\text{ g/cm}^3$) is less than half that of WHAs ($\sim 16.5\text{--}18.5\text{ g/cm}^3$), restricting their use in applications that demand high inertia, penetration, or shielding. The stark density-mechanical property trade-off between WHAs and UHSSs motivates the exploration of new materials that can bridge this performance gap.

Recently, Ni–W based medium heavy alloys (MHAs) have emerged as promising candidates to fill this niche. By combining the high density of W with the excellent deformability of face-centered cubic (FCC) nickel (Ni), MHAs exhibit a unique balance of density and mechanical performance. Our previously developed prototype Ni–W based MHA with a composition of 57Ni–37W–5Co–1Ta (in wt%) demonstrates this balance effectively [14]. With the Ni–W solid solution-based FCC matrix, the prototype MHA ($\sim 11.39\text{ g/cm}^3$) achieves higher density than UHSSs while offering superior mechanical performance compared with traditional UHSSs [15, 16]. Unlike BCC-structured WHAs, which intrinsically suffer from limited deformability, our prototype and subsequently developed MHAs features a single-phase FCC Ni–W solid-solution matrix [14, 17]. This FCC matrix not only improves intrinsic deformability but also enables additional potential strengthening through deformation-induced mechanisms and potential secondary-phase precipitation. This distinctive microstructural framework highlights Ni–W based MHAs as a new

generation of alloys with significant potential in defense, aerospace, and energy-intensive industries.

An intriguing feature of Ni–W based alloys, as revealed in our prior studies, is the presence of SRO, which was observed in the forged condition and evolved into ordered Ni₄W precipitates upon post-aging treatment [14]. SRO is a fundamental structural phenomenon in solid solutions, characterized by non-random atomic arrangements over a few interatomic distance, which can profoundly influence the materials’ thermodynamic stability [18], stacking fault energy [19, 20], irradiation response [21, 22], corrosion resistance [23], and mechanical behavior [24, 25]. In FCC alloys, SRO has been reported to alter dislocation behavior, enhance solution strengthening, and in some cases act as a precursor to long-range ordered phases [26–28]. However, despite its significance, the understanding of SRO in Ni–W based MHAs remains incomplete. In particular, the role of W concentration in governing the degree of SRO, as well as its correlation with strengthening mechanisms and overall alloy performance, has not yet been systematically clarified. This knowledge gap is particularly important in the context of alloy design. For MHAs to evolve into a technologically viable class of materials, it is critical to establish a mechanistic understanding of the factors controlling SRO formation and stability. Concentration-dependent SRO behavior is especially relevant because the solute–solute interactions, lattice strain, and chemical bonding introduced by W atoms directly affect both the local ordering tendency and the resulting solution strengthening. A deeper comprehension of these effects will not only enable the rational design of Ni–W based alloys with optimized performance but also inform broader alloy development strategies across FCC-based medium- and high-density systems.

In this work, we aim to systematically investigate the influence of W concentration on SRO formation, solution strengthening, and microstructural evolution in Ni–W alloys upon deformation. By combining advanced characterization techniques, including synchrotron X-ray diffraction, transmission electron microscopy (TEM), atom probe tomography (APT), and advanced theoretical calculations—with systematic evaluations of mechanical performance, we reveal the intrinsic role of W in governing SRO behavior and the consequent effects on mechanical performance. The correlation among W concentration, SRO, and strengthening response is established. The insights gained not only advance the fundamental understanding of SRO in Ni–

W systems but also provide a knowledge base for the design of next-generation MHAs that bridge the density and performance gaps between WHAs and UHSSs.

2. Experimental procedures and theoretical calculations

The Ni-W binary alloys with varying W contents were prepared using the vacuum induction melting method. The nominal W contents were 0%, 10%, 20%, 30%, 34%, and 38% (in wt.%), designated as Ni, Ni-10W, Ni-20W, Ni-30W, Ni-34W, and Ni-38W, respectively. After melting, the alloys were cast into ingots, reheated to 1200 °C, and subjected to multiple forging passes to produce rods with a diameter of 20 mm. The forged alloys were subsequently solution-treated at 850 °C, 900 °C, 950 °C, 1000 °C, 1050 °C, and 1100 °C for 1h, followed by water quenching. For optical microscopy observations, samples were mechanically grounded, polished, and etched using a solution containing 2 g CuCl₂, 40 mL HCl, and 60 mL ethanol. Tensile tests were carried out at room temperature on the INSTRON 5582 testing machine at a strain rate of $5 \times 10^{-4} \text{ s}^{-1}$. The tensile specimens had a standard geometry with a gauge section diameter of 5 mm, and a gauge length of 25 mm. X-ray diffraction (XRD) analyses were performed using a Bruker D8 diffractometer with Cu radiation ($\lambda=1.541 \text{ \AA}$). Synchrotron radiation XRD measurements were conducted at the BL13SSW beamline of the Shanghai Synchrotron Radiation Facility using the photon energy of 50 keV ($\lambda=0.248 \text{ \AA}$) and 97.9 keV ($\lambda=0.127 \text{ \AA}$). TEM characterizations were carried out on the ARM 200CF microscope equipped with a probe lens corrector. The microscope was operated at 200 kV. Electron transparent thin foils were prepared by conventional ion milling. Three-dimensional APT was employed to investigate the grain boundary chemistry of Ni–W alloys using a CAMECA local electrode atom probe (LEAP) 5000XS instrument with a detection efficiency of approximately 80%. The APT datasets were collected in laser pulsing mode at a base temperature of 50 K, with a laser pulse energy of 30 pJ and a pulse frequency of 250~500 kHz. Three-dimensional reconstructions and data analysis were processed with the AP Suite 6.3 software package. Needle-shaped specimens for APT analysis were prepared using a Thermo Fisher Helios 5 plasma focused ion beam (FIB) system equipped with a Xe source and electron backscatter diffraction (EBSD) detector. To identify the grain boundary (GB) located near the specimen's apex and misorientation angles across GBs, transmission Kikuchi diffraction (TKD) was also performed after FIB sharpening using an Oxford Symmetry S3 detector with an accelerating voltage of 25 kV, probe current of 1.6 nA, and step size of 5 nm.

First-principles thermodynamic calculations were performed to investigate the origin and characteristics of SRO in Ni-W alloys. Cluster expansion (CE) coupled with Monte Carlo (MC) simulations were performed to predict the SRO tendency of the system. In this work, we used a recently developed Bayesian CE method implemented in the Alloy Theoretical Automatic Toolkit (ATAT) [29-32]. This approach ensures an exact fit for all ground states by construction while significantly reducing the computational cost. Since FCC W is mechanically unstable, the inflection detection method was applied to obtain the precise reference energy [33-35]. To train the CE model, 30 structures near the Ni-rich end of the Ni-W system were selected as references configurations. First-principles calculations were carried out using the Vienna *ab initio* Simulation Package (VASP) [36-39], employing the projector augmented wave (PAW) method and the Perdew–Burke–Ernzerhof (PBE) exchange-correlation functional, with an energy cutoff of 520 eV [39-41]. K-point meshes were automatically generated through ATAT to ensure a minimum density of 2000 k-points per reciprocal atoms [29].

Following the CE construction, MC simulation was conducted to determine the phase boundaries and SRO evolution up to 20 at% of W. The *phb* module in ATAT [29] was first used to predict the two-phase region separating FCC Ni and Ni₄W. Equilibrium atomic correlations were then obtained using the *memc2* code [29], and the corresponding cluster concentrations were derived using the V-matrix formalism [42], which was implemented in the *cvmclus* module in ATAT [43]. To quantify SRO in the Ni-W system, the Warren-Cowley SRO parameter was calculated as [44]:

$$\alpha_{ij} = 1 - \frac{P_{ij}}{2c_i c_j} \quad (1)$$

where α_{ij} is the SRO parameter for the nearest neighbor pair $i-j$, P_{ij} is the probability of finding such a pair among all first nearest neighbor pairs, and c_i and c_j are the atomic fractions of elements i and j , respectively. The SRO parameters are computed for various temperature-composition conditions using MC simulations, and the resulting Warren-Cowley SRO heat map was superimposed on the conventional phase diagram to construct the SRO phase diagram of the Ni-W system.

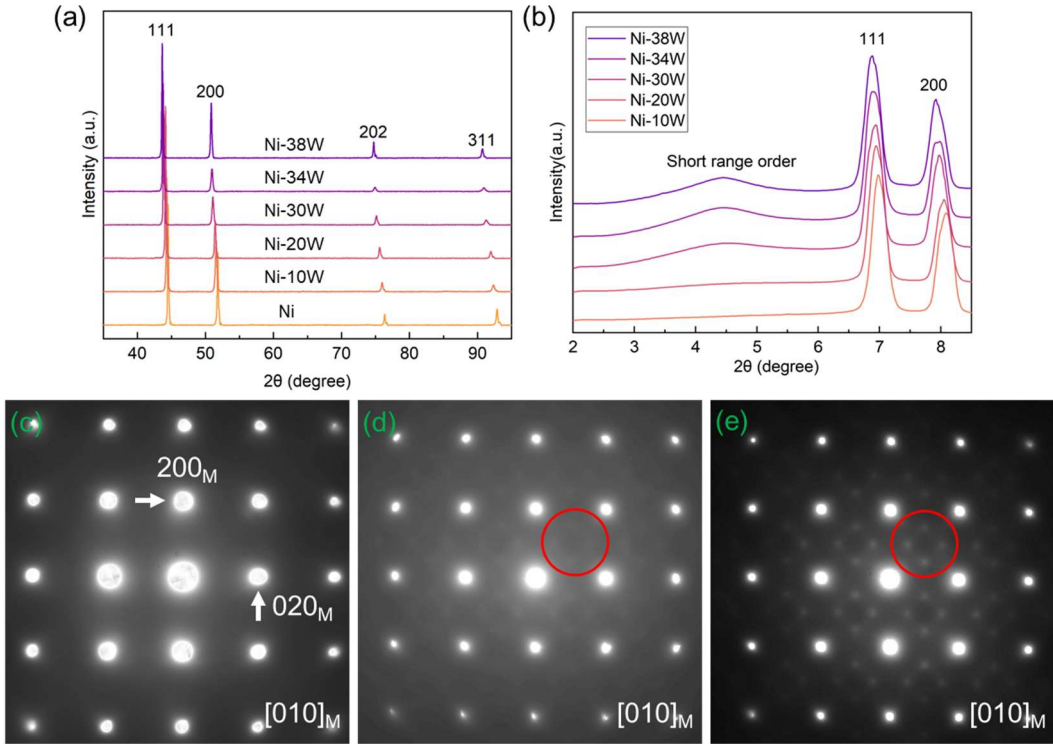


Figure 1. (a) Traditional XRD results of various Ni-W alloys. (b) Low angle synchrotron radiation XRD results of Ni-W alloys with varied W contents. Selected area electron diffraction (SAED) patterns of (c) Ni-10W, (d) Ni-30W, (e) Ni-34W samples. The arrows in (d, e) indicate the satellite patterns. All alloys investigated here were solution-treated at 1050°C for 1h.

3. Results

3.1 Concentration-dependent SRO behavior

Across all investigated W contents, the solution-treated Ni-W alloys exhibit a single-phase FCC structure, as confirmed by XRD patterns in **Fig. 1a**. Synchrotron radiation XRD data (**Fig. 1b**) reveal broad diffusion peaks around 4.5° in alloys with W concentration exceeding 30%. The intensity of these diffuse peaks increases with higher W concentration, indicating the progressive development of SRO. The SAED patterns in **Figs. 1c-e** correspond to Ni-10W, Ni-30W and Ni-34W, respectively, all of which can be indexed along the $[001]_M$ zone-axis, where the subscript M denotes the FCC Ni-W matrix. Compared to **Fig. 1c**, distinct satellite patterns at $\{110\}_M$ are observed in **Figs. 1d** and **1e**, conforming the formation of SRO within the solid-solution matrix

[14, 45]. Furthermore, the satellite reflections in Ni-34W are noticeably stronger than those in Ni-30W, consistent with the bulk XRD observations.

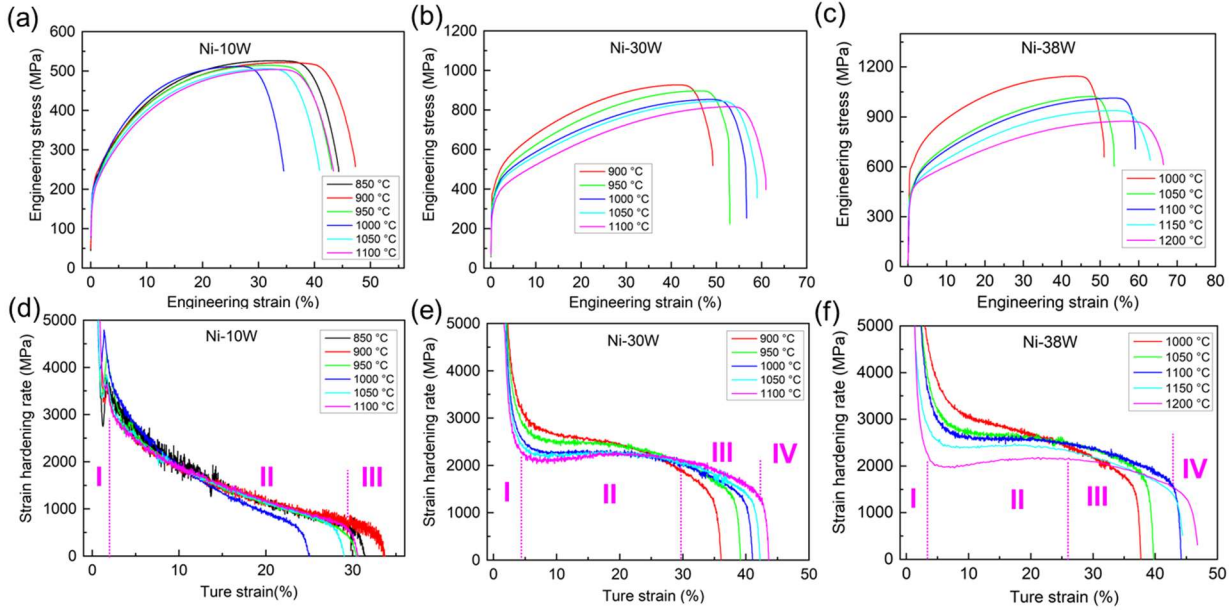


Figure 2. Engineering stress-strain and strain hardening rate curves of Ni-W alloys at different solution temperatures. (a, d) Ni-10W, (b, e) Ni-30W, (c, f) Ni-38W. The solution temperature for each curve is indicated in the legend. The vertical pink dash lines in (d-f) highlight the distinct deformation stages for Ni-10W solution-treated at 1100 °C, Ni-30W solution-treated at 1100 °C and Ni-38W solution-treated at 1200 °C respectively.

3.2 Concentration-dependent mechanical behavior

To elucidate the effect of W on grain-refinement strengthening, a series of solution treatments at different temperatures were performed on Ni-W alloys with varying W contents, followed by optical microscopy characterizations (Supplementary Figs. S1-S5). The results indicate that the recrystallization temperature increases with W concentration. Alloys containing less than 30 wt.% W were fully recrystallized at 900 °C, whereas Ni-34W and Ni-38W required higher temperatures of 950 °C and 1000 °C, respectively. Grain growth occurred at temperatures above the recrystallization threshold, with higher-W alloys exhibiting slower grain coarsening kinetics. The measured grain sizes for each alloy are summarized in Table S1.

Tensile stress-strain curves and strain-hardening rate plots for various alloys subjected to different solution-treatment temperatures, are presented in Fig. 2 and Supplementary Fig. S6. The variations of yield strength (YS), ultimate tensile strength (UTS) and elongation of Ni-W alloys

with different W concentrations and solution temperatures are summarized in **Table S2-S4**. Both YS and UTS increase markedly with W content. However, increasing the solution-treatment temperature leads to reductions in YS and UTS due to recrystallization and subsequent grain growth. **Fig. 2d** and **Fig. S6c** are the strain-hardening rate ($\theta = \frac{d\sigma}{d\epsilon}$) versus true strain curve of Ni–W alloys with lower W concentrations (<30 wt%) and negligible SRO features. It is found that their deformations exhibit three characteristic strain-hardening stages. Taking Ni-10W treated at 1100 °C as an example (**Fig. 2d**), Stage I (0–2.5% strain) shows a rapid decrease in θ accompanied by a sharp increase in true stress. In Stage II (2.5–28% strain), the curve displays a quasi-linear relationship in which true stress continues to rise, albeit more gradually, while θ steadily declines. When the strain exceeds ~28%, Stage III begins, where θ decreases to zero or negative values promptly, signaling the onset of plastic instability and non-uniform deformation. In contrast, for alloys with higher W contents (≥ 30 wt%) and evident SRO features, the strain-hardening behavior becomes distinctly four-staged (**Figs. S6d, 2e, 2f**). After the initial rapid decrease in θ during Stage I, a pronounced plateau appears and persists through most of the deformation process. In this regime, θ remains nearly constant or slowly declines, reflecting a dynamic balance between defects storage and recovery. For Ni-30W treated at 1100 °C (**Fig. 2e**), the plateau extends from approximately 5–30% strain (about 55% of the total deformation), while for Ni-38W heated at 1200 °C (**Fig. 2f**), it spans 4–27% strain (about 49% of total deformation). Beyond the plateau, both Ni-30W and Ni-38W exhibit dynamic recovery and softening like those in Ni-10W (**Fig. 2d**) and Ni-20W (**Fig. S6c**). This evolution highlights the critical role of SRO in governing the deformation mechanisms and strain-hardening behavior of Ni–W alloys.

The mechanical behavior of Ni–W alloys is strongly governed by W concentration, solution-treatment temperature, and grain size. As shown in **Fig. 3a**, Yong's modulus, density and lattice parameters all increase linearly with W content. The dominant strengthening mechanisms in these alloys are solid-solution and GB hardening, while contributions from precipitation and dislocation strengthening are negligible in recrystallized alloys. This is because deformation-induced defects introduced during forging are fully recovered, and no long-range ordered Ni₄W precipitates are detected in the solution-treated alloys. GBs strengthening follows the Hall-Petch relationship: $\sigma_y = \sigma_0 + k_y d^{-\frac{1}{2}}$, where σ_y is the yield strength, σ_0 is the friction stress for dislocation slip, d is the grain size, and k_y is the Hall-Petch coefficient quantifying the effect of grain size on yield

strength [46-49]. As shown in **Fig. 3b**, YS scales linearly with $d^{-\frac{1}{2}}$ for all alloys, and both σ_0 and k_y increase with W content. At 38% W, the Hall-Petch coefficient k_y reaches an exceptionally high value of $\sim 1102 \text{ MPa} \cdot \mu\text{m}^{-\frac{1}{2}}$, exceeding nearly all previously reported values [50, 51]. For comparison, the Ni-Mo system exhibits a maximum k_y of $\sim 1028 \text{ MPa} \cdot \mu\text{m}^{-\frac{1}{2}}$ at the Mo's solubility limit [50]. The relative evolution of σ_0 and k_y with increasing W content is shown in **Fig. 3c**. The variations of both parameters can be divided into two distinct stages, with a transition occurring around 30 wt.% W — corresponding to the threshold for significant SRO formation. Beyond this transition, the increase in k_y becomes markedly more pronounced, while the growth rate of σ_0 slows compared to the initial stage without SRO. This two-stage behavior indicates that SRO plays a crucial role in governing the deformation mechanisms of Ni-W alloys process.

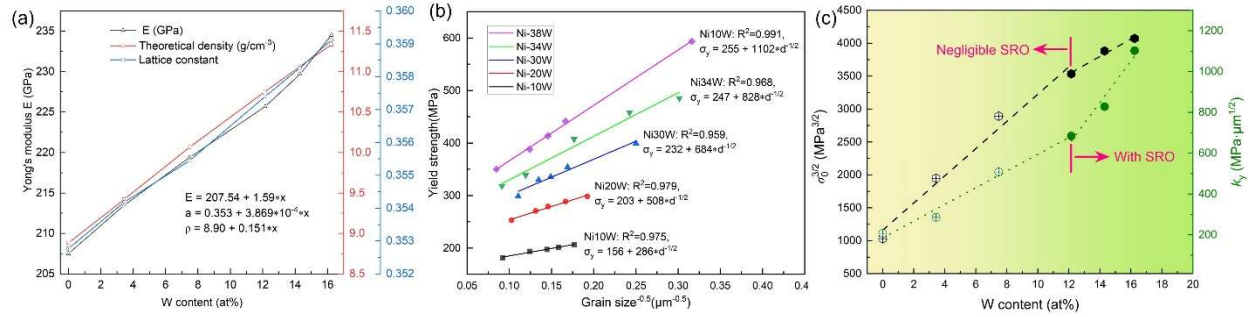


Figure 3. (a) Variation of Yong's modulus, theoretical density and lattice constant for Ni-W binary alloys as W content increases. (b) Hall-Petch relationships of Ni-W binary alloys with different W contents. The fitted curves for each alloy are indicated. (c) Variation of original yield stress $\sigma_0^{3/2}$ and Hall-Petch constants k_y as W content increases.

3.3 Microstructural features of Ni-W alloys

To investigate the influence of W concentration on GB chemistry, APT analyses were conducted on Ni-10W (solution-treated at 1000 °C) and Ni-38W samples (solution-treated at 1100 °C) alloys with comparable grain sizes. **Figs. 4a** and **4b** show the corresponding IPF maps, and site-specific APT needles were extracted from the regions marked as ROI. Correlative TKD-APT analyses (**Figs. 4c** and **4d**) confirm that the selected GBs in both Ni-10W and Ni-38W possess comparable crystallographic character, each corresponding to a high-angle grain boundary (HAGB) with misorientations of 50° and 48°, respectively. **Fig. 5a** displays the 3D atom maps and 2D ion-density plots of Ni and W for the Ni-10W sample. Although the 3D maps reveal no apparent

segregation or depletion, the 2D density plot shows a positional shift of low-density regions associated with crystallographic zone lines (highlighted by black arrows) from the upper to lower regions, indicating the presence of a GB (**Figs. 4a** and **4c**). The 1D composition profile across the GB shows slight W depletion accompanied by Ni enrichment at the GB (**Fig. 5b**), suggesting that W exhibits weak boundary affinity at low concentrations. In contrast, as shown in **Figs. 5c** and **5d**, the Ni-38W sample exhibits clear Ni depletion and pronounced W enrichment at a HAGB with the misorientation angle of 48° , indicating a strong segregation tendency at higher W contents. The 1D composition profile quantifies the peak GB W concentration to be ~ 24 at.%. Slightly W-depleted zones adjacent to the GB (indicated by arrows) suggests that W atoms diffused toward the boundary during solution treatment [52]. This reversal in segregation with increasing W concentration is likely linked to the emergence of SRO. SRO likely modifies the local bonding environment and increases elastic strain energy near GBs. The W segregation provides a mechanism to partially relax this strain, thereby promoting enrichment of W at the boundaries in Ni-W alloys.

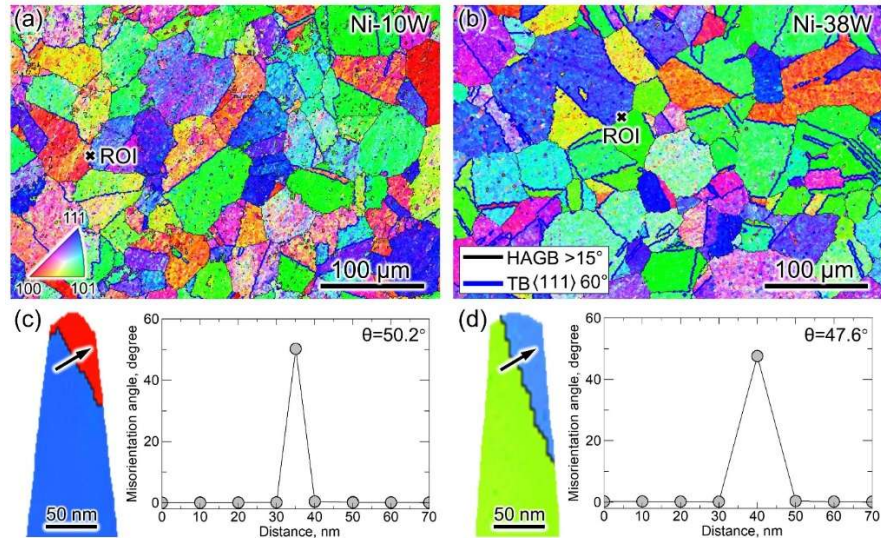


Figure 4. (a, b) EBSD inverse pole figure (IPF) maps showing the grain boundaries (GBs) selected for site-specific APT specimen preparation, indicated by region of interest (ROI) cross marks; and (c, d) TKD IPF maps along with corresponding misorientation angle profiles across the GBs indicated by arrows, for Ni-10W and Ni-38W samples solution-treated at 1000 °C and 1100 °C, respectively.

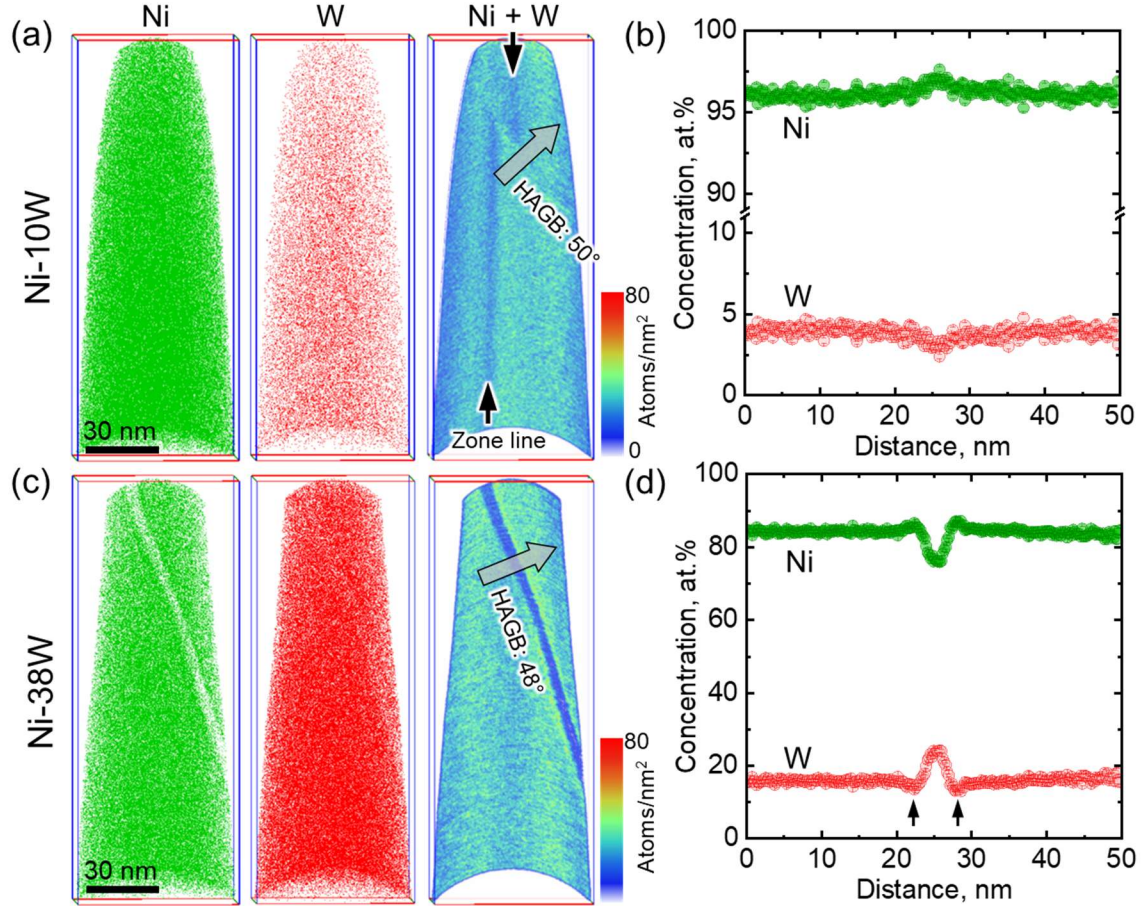


Figure 5. (a, c) 3D atom maps and 2D ion density plots of Ni and W; and (b, d) 1D composition profiles across the grain boundaries along the cylindrical regions (30 nm in diameter) indicated by grey arrows in (a) and (c), for Ni-10W and Ni-38W samples solution-treated at 1000 °C and 1100 °C, respectively. Note that the black arrows in (a) indicate low-density regions corresponding to crystallographic zone lines.

To elucidate the effect of W concentration on the deformation microstructures of Ni-W alloys, systematic synchrotron X-ray experiments were conducted on Ni-10W (solution-treated at 1000 °C) and Ni-38W (solution treated at 1100 °C) samples with comparable grain size, subjected to different levels of deformation. The dislocation density was estimated using the classical Williamson–Hall method, which relates diffraction peak broadening to both grain size and microstrain [53]. Diffraction peaks were fitted using Gaussian functions to determine the full width at half maximum (FWHM), and the strain contribution was analyzed through K – ΔK plots, where $K = \frac{1}{d} = \frac{2\sin\theta}{\lambda} = \frac{Q}{2\pi}$, $\Delta K = \frac{\cos\theta * \Delta 2\theta}{\lambda} = \frac{\Delta Q}{2\pi}$. Here, θ is the diffraction angle, Q is the reciprocal

lattice vector, λ is the X-ray wavelength, d is the interplanar spacing, and $\Delta 2\theta$ is the FWHM in real space. If peak broadening arises solely from grain size, the $K-\Delta K$ plot appears as a horizontal line; if dominated by strain, the line passes through the origin. When both effects contribute, the plot intersects the y -axis positively. The microstrain (ε) can be further related to dislocation density as $\rho = B(\frac{\varepsilon}{b})^2$, where B is a constant dependent on material properties and dislocation configuration [53].

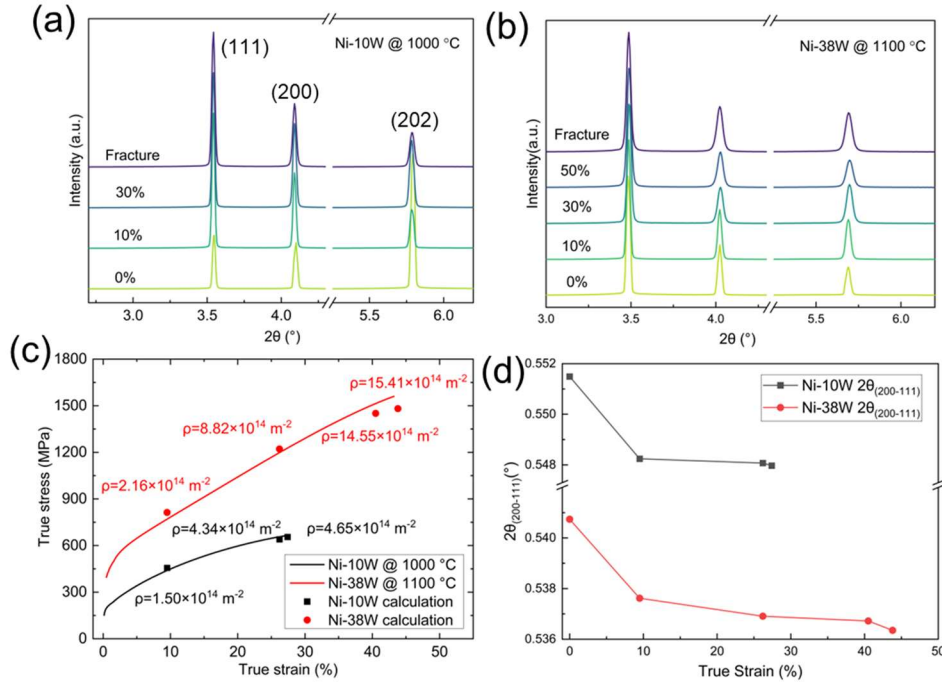


Figure 6. Synchrotron radiation XRD of (a) Ni-10W and (b) Ni-38W under various degrees of deformation. (c) True stress–strain curves and corresponding calculated values for Ni-10W and Ni-38W. (d) Comparisons of 2θ difference between (200) and (111) peak for Ni-10W and Ni-38W alloys. The used photon energy here is 50 keV.

To correct for instrumental broadening, CeO_2 powder was used as a standard sample (Fig. S7a), as its intrinsic macrostrain is negligible. Gaussian fitting of each diffraction peak — illustrated by the (200) peak in Fig. S7b — provided FWHM values used to construct $K-\Delta K$ plots (Fig. S7c). The same analysis procedure was applied to Ni-W alloys. Figs. 6a and 6b shows the synchrotron radiation XRD profiles of Ni-10W and Ni3-8W alloys at various deformation levels, with the corresponding $K-\Delta K$ plots presented in Figs. S7d and 7e. For fractured samples, the true strain corresponds to the maximum true stress, as specimens were taken from regions distant from

the fracture surfaces. In both Ni-10W and Ni-38W alloys, the slope of $K-\Delta K$ plots increased with deformation (**Figs. S7d** and **7e**), indicating a progressive rise in dislocation density. Notably, Ni-38W exhibited a more pronounced slope increase than Ni-10W, signifying enhanced dislocation accumulation. The true stress-strain curves and calculated dislocation densities for both alloys are shown in **Fig. 6c**. Quantitative analysis reveals that Ni-38W possesses significantly higher dislocation densities than Ni-10W — approximately 1.44× and 2.03× greater at 10% and 30% strain, respectively—and this difference further widens to ~3.31× at fracture. The strain-hardening behavior of Ni–W alloys was further examined using the Taylor model, which relates the increment in strain-hardening (σ_p) to dislocation density (ρ) via dislocation interactions:[54] $\sigma_p = M\alpha GbB\rho^{0.5}$, where M is the Taylor factor (~3.06 for FCC metals), α is a fitting constant reflecting the strength of dislocation interactions, G is the shear modulus, and b is the Burgers vector. Based on a Poisson's ratio of ~0.31, the shear modulus values for Ni-10W (solution-treated at 1000 °C) and Ni-38W (solution-treated at 1100 °C) are ~89.5 GPa and ~81.5 GPa, respectively, and the corresponding Burgers vectors are 0.2504 nm and 0.2539 nm. The fitted α values, which are indicative of dislocations uniformity interactions [55], are ~ 0.338 for Ni-10W and ~0.391 for Ni-38W. This demonstrates that dislocations are more uniform, and dislocation interactions are much stronger in Ni-38W compared to Ni-10W. Consequently, even at comparable dislocation densities, Ni-38W exhibits a larger strengthening increment, underscoring the critical role of dislocation configuration and uniformity in its superior strain-hardening behavior.

Besides dislocations, planar defects such as stacking faults and twins also play important roles in accommodating microscopic deformation. Since planar defects alter the interplanar spacings anisotropically in FCC metals, the (111) reflection—whose plane coincides with the typical fault plane {111}—is particularly sensitive to their presence, while the (200) reflection is less affected. Therefore, the 2θ separation between the (111) and (200) diffraction peaks can serve as a qualitative indicator of the relative stacking fault energy (SFE) [56-58]. To evaluate the influence of W concentrations on the SFE, we analyzed the 2θ separation between the (111) and (200) peaks of Ni-10W (solution-treated at 1000 °C) and Ni-38W (solution-treated at 1100 °C) to estimate the planar defects probability. As shown in **Figs. 6a** and **6b**, with increasing deformation, the (111) diffraction peak gradually shifts toward higher angles, while the (200) peak remains nearly unchanged. **Fig. 6d**, derived from **Figs. 6a** and **4b**, illustrates the variation in the 2θ difference between the (111) and (200) peaks for Ni-10W and Ni-38W alloys under different deformation levels. At a true strain of

10%, both alloys exhibit a reduced angular difference, indicating the formation of stacking fault. As deformation increases further, the angular difference in Ni-10W becomes nearly constant, suggesting that stacking faults formation saturates beyond 10% strain. In contrast, Ni-38W continues to show a progressive reduction in the 2θ difference, implying continuous accumulation of stacking faults with increasing strain.

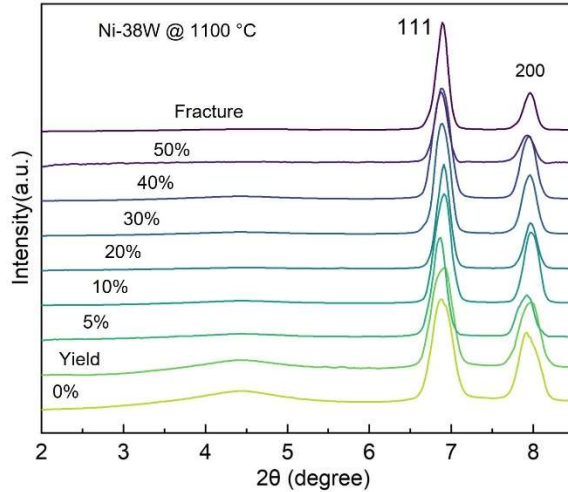


Figure 7. Synchrotron radiation XRD of Ni-38W alloy subjected to different strain stages. The used photon energy is 97.9 keV.

Fig. 7a corresponds to the synchrotron XRD patterns of Ni-38W at various deformation levels obtained at the low-angle range. It is clearly shown that SRO features—manifested as a broad peak around 4.5° —disappears after yielding, suggesting that SRO regions can be destroyed by dislocation shear. To further elucidate the effect of SRO on the deformation mechanisms with higher spatial resolution, detailed TEM analyses were performed on Ni-10W and Ni-38W alloys subject to varying deformation levels. As shown in **Figs. 8a-d** and Supplementary **Fig. S8**, in Ni-W alloys without negligible SRO, dislocations are initially activated and progressively accumulated with increasing strain, eventually forming typical dislocation cell structures (highlighted by the dashed frames). In contrast, the Ni-38W alloy exhibiting SRO features shows pronounced plane slip along $\{111\}$ planes, leading to the formation of distinct shear bands, as illustrated in **Figs. 8e-g**. Upon further deformation toward fracture, strain localization within these shear bands promotes the development of stacking faults and micro-twins, as observed in **Figs. 8h** and **9**.

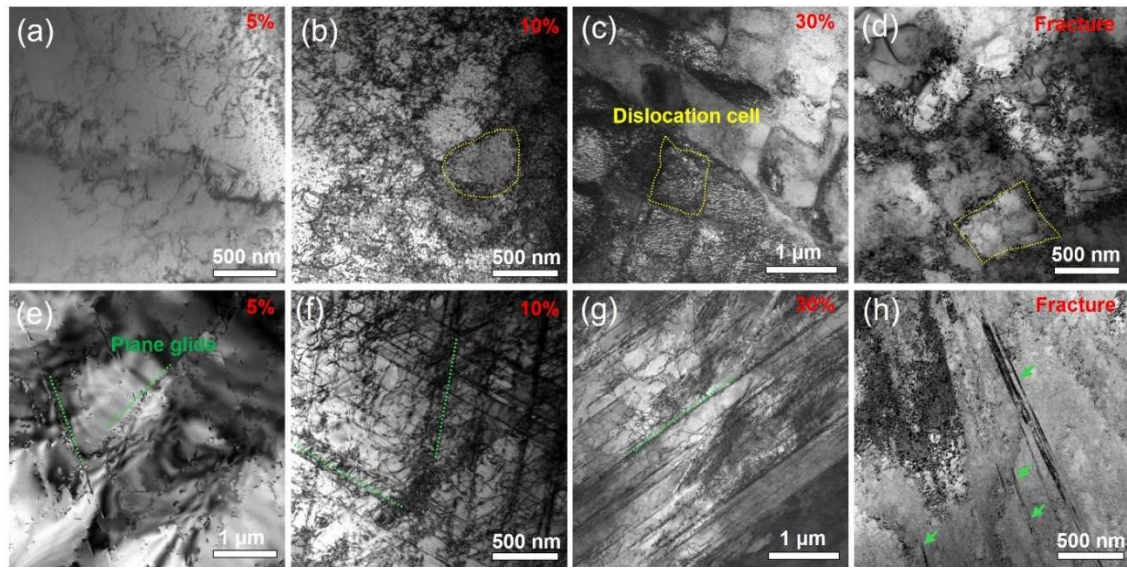


Figure 8. TEM image of the (a-d) Ni-10W solution-treated at 1000 °C and (e-h) Ni-38W solution-treated at 1100 °C under different deformation conditions. The dotted yellow frames indicated in (b-d) indicate the formation of dislocation cell structure. The dotted lines in (e-g) indicate the plane glide on {111}. The arrows in (h) indicate the formation of nanosized twin.

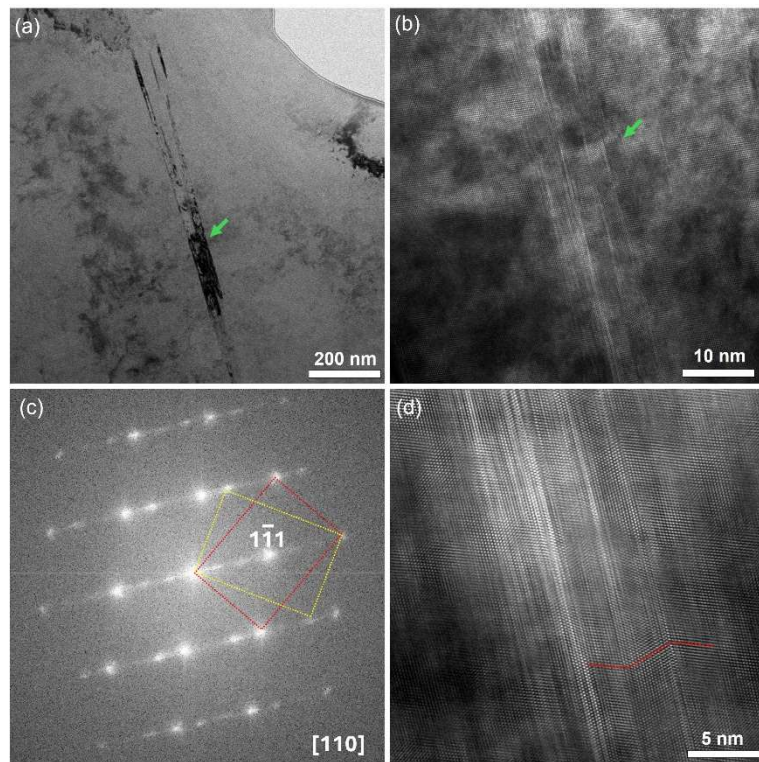


Figure 9. (a) TEM image and (b) High resolution TEM image of the Ni-38W alloys solution-treated at 1100 °C under fracture conditions. The arrows indicate the nanosized twin. (c) Digital Fast Fourier transformed patterns corresponding to HRTEM image shown in (b). The dotted frames highlight the twining structure. (d) Localized magnification of HRTEM image shown in (b). The dotted lines indicate the twinning features at the atomic scale.

4. Discussion

4.1 Origin of SRO in Ni-W alloys

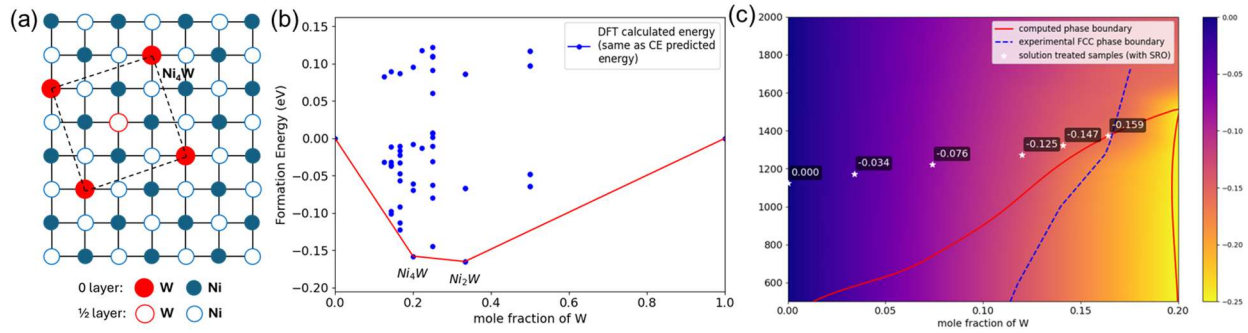


Figure 10. (a) Structure of Ni₄W on FCC lattice. (b) The Ni-rich convex hull of FCC Ni-W system (with FCC W as the reference state). (c) The SRO phase diagram of Ni-rich region compared with experimental FCC phase boundary [59].

The origin of SRO in the Ni-W binary system can be elucidated through first-principles thermodynamic analysis, as shown in **Fig. 10**. As shown in, the calculated convex hull of the reference structures predicts two ground states (**Fig. 10b**): D0₁₉-Ni₄W and Pt₂Mo-Ni₂W [60]. Among these, only the Ni₄W phase is relevant under equilibrium conditions, as Ni₂W possesses a higher W concentration and cease to be a global ground state when BCC W is used as reference. The Ni₄W phase exhibits a FCC-based structure, as illustrated in **Fig. 10a**, which is the structural template of the SRO observed in Ni-W alloys. Based on these reference structures, a CE model was constructed with a cross-validation (CV) score of 0.014 eV, which is reasonable for the Ni-W system considering its significant lattice mismatch (14.5% in lattice parameters). It is noted that only Ni-rich structures were included in the current CE construction. The discrepancy between the MC-predicted FCC phase boundary and experimental CALPHAD boundary likely originates from the neglect of long-range elastic and vibrational contributions in the present CE formulation [61].

The resulting SRO phase diagram, shown in **Fig. 10c**, reveals a clear compositional dependence of the SRO parameters. The detailed procedure for SRO phase diagram generation is

included in the note in Supplementary Materials. As the W content increases from 20 wt.% to 30 wt.%, the SRO parameter for the disordered FCC phase decreases substantially from -0.08 to -0.14, signifying an enhanced degree of SRO and those exhibiting pronounced local ordering. This SRO parameter change corroborates with the observed threshold (\sim 30 wt.% W) for significant SRO formation in our experiments. Such variations in the extent of SRO have a profound impact on deformation behavior, as evidenced by the corresponding experimental observations (**Figs. 2d-f, 3c**). It is important to note that the present SRO analysis relies on equilibrium thermodynamics and omits kinetic effects associated with processing, solution treatment, and quenching. Despite this limitation, the analysis is expected to qualitatively reflect the overall trends of SRO formation in Ni–W alloys.

4.2 Effect of W concentration and SRO on friction stress and Hall–Patch coefficient

As shown in **Fig. 3c**, both σ_0 and k_y increase with W concentration, reflecting the progressive strengthening of Ni–W alloys through solid-solution and grain boundary effects. However, their respective rates of increase exhibit distinct concentration-dependent behaviors associated with the emergence of SRO. At low W contents (<30 wt%), the alloy behaves as a conventional solid solution, where solute–dislocation interactions arising from atomic size and modulus mismatches dominate strengthening. In this regime, σ_0 and k_y increase moderately with W addition, consistent with classical solid-solution and grain boundary strengthening mechanisms.

When the W concentration exceeds \sim 30 wt.%, SRO becomes evident, leading to a notable divergence in the evolution of σ_0 and k_y . The evolution of σ_0 with W addition shows a smaller incremental slope in the SRO regime. While SRO increases the local lattice resistance to dislocation motion through periodic atomic ordering, it simultaneously reduces random solute–dislocation interactions that dominate conventional solid-solution hardening. This partial ordering thus stabilizes the lattice and limits the further rise of σ_0 . In contrast, the Hall-Patch slope k_y exhibits a steep rise, whereas the increase in friction stress σ_0 becomes more gradual. This contrasting behavior originates from the distinct ways in which SRO affects dislocation and GB interactions. The formation of SRO, manifested as periodic, compositionally correlated arrangements of Ni and W atoms, induces spatially coherent lattice distortions that hinder dislocation glide and intensify local stress concentrations near grain boundaries. The concurrent reduction in SFE, coupled with the presence of SRO, promotes planar dislocation glide while

suppressing cross-slip, leading to severe dislocation pileups at GBs. These pile-ups elevate local back-stresses and increase the resistance to slip transmission across boundaries, resulting in a substantial enhancement of k_y . Moreover, the observed W enrichment along GBs in high-W alloys (**Figs. 5b** and **5d**) further amplifies GB strengthening by increasing the stress required for dislocation transmission, enhancing solute drag and back-stress effects, and altering GB structural units. These solute segregation effects act synergistically with SRO-induced planar slip and reduced SFE to produce a super-additive increase in the Hall–Petch coefficient k_y , thereby explaining the pronounced nonlinear strengthening behavior observed beyond the SRO threshold.

4.3 Correlation between microstructure and deformation behavior

The present study provides direct experimental evidence linking SRO to the deformation behavior of Ni–W alloys. The mechanical response and corresponding microstructural evolution reveal that SRO exerts a pronounced influence on dislocation activity, strain hardening behavior, and defect formation mechanisms. These findings elucidate the fundamental role of local chemical ordering in governing the deformation pathways of concentrated solid-solution alloys. At the early stage of deformation, the presence of SRO in the Ni–38W alloy impedes the motion of dislocations by locally pinning them, thereby elevating the initial yield stress. This behavior is consistent with the higher critical resolved shear stress often observed in SRO-containing solid solutions. The strain-hardening rate versus strain curves exhibits four distinct stages, among which a characteristic plateau is particularly evident in the SRO-containing alloy. However, synchrotron XRD data indicate that SRO features rapidly diminish after yielding (**Fig. 7**), suggesting that the SRO domains are disrupted by intense dislocation glide and local lattice shearing. Therefore, the observed plateau should not be attributed solely to the sustained presence of SRO, but rather to the strong dislocation–dislocation interactions and the subsequent planar slip that emerge after the initial breakdown of SRO.

The distinct differences in deformation microstructures between Ni–10W and Ni–38W provide further insight into the role of W concentration and SRO in controlling deformation modes. In the Ni–10W alloy, which exhibits relatively weak SRO and higher SFE, deformation proceeds primarily through the accumulation and entanglement of dislocations, leading to the formation of typical dislocation cell structures (**Figs. 8a-d** and **S8**). In contrast, the Ni–38W alloy, characterized by pronounced SRO and relatively lower SFE, displays a transition from dislocation activation to planar slip along $\{111\}$ planes, followed by the development of shear bands, stacking faults, and

nanotwins at higher strains (**Figs. 8e-h** and **Fig. 9**). The emergence of planar glide in Ni–38W can be rationalized by the presence of SRO, which promotes localized slip along specific crystallographic planes by restricting cross-slip and homogenized dislocation motion. Once planar glide is activated, the dislocation arrays on parallel planes strongly interact, giving rise to dense shear bands and facilitating the nucleation of stacking faults and twins. This sequential evolution aligns well with the distinct strain-hardening stages, where the initial strengthening is dominated by SRO-related lattice friction, the intermediate plateau corresponds to strong planar dislocation interactions, and the later stage is governed by twin-mediated hardening before the onset of softening. The disappearance of SRO during deformation can be attributed to the cumulative effect of dislocation movement and localized shear strain. The passage of dislocations redistributes solute atoms and disrupts the energetically favorable short-range configurations, thereby destroying the local order that initially impeded slip. Once SRO is eliminated, deformation proceeds via mechanisms characteristic of random solid solutions, including dynamic recovery and dislocation rearrangement. This transformation from SRO-controlled to dislocation-interaction-controlled deformation provides a natural explanation for the transition in strain-hardening behavior.

5. Conclusions

In summary, this study reveals that the formation of Ni_4W -like SRO in Ni–W alloys is strongly dependent on W concentration, with a threshold near ~ 30 wt%. This threshold corroborates with the Ni–W SRO phase diagram predicted by first-principles thermodynamics. Below this threshold, alloys have low SRO and deform predominantly through dislocation cell structures. As W content increases, the SFE decreases, promoting SRO formation, and transitioning the deformation mode toward planar glide accompanied by stacking faults and deformation twins. SRO also exerts a pronounced influence on the Hall–Petch relationship. Beyond the SRO threshold, enhanced defect–grain boundary interactions lead to a steep, nonlinear rise in the Hall–Petch slope (k_y), whereas the increase in friction stress (σ_0) becomes more gradual. This contrast indicates that SRO more effectively strengthens grain boundary–related mechanisms than intrinsic lattice resistance. Additionally, Ni–W alloys containing SRO exhibits a characteristic plateau occupying most of the deformation stage in the strain-hardening rate versus strain curve, reflecting a sustained balance between hardening and softening throughout deformation. Overall, W concentration and the associated development of SRO play a pivotal role in governing the deformation behavior and mechanical stability of Ni–W alloys. These insights provide valuable

guidance for the compositional and microstructural design of next-generation Ni–W–based MHAs, enabling optimized combinations of density, strength, ductility, and toughness for advanced structural applications.

Acknowledgments

We acknowledge the Shanghai Synchrotron Radiation Facility for the X-ray diffraction experiments. This work also made use of the EPIC facility (RRID: SCR_026361) of Northwestern University's NUANCE Center, which has received support from the SHyNE Resource (NSF ECCS-2025633), the IIN, and Northwestern's MRSEC program (NSF DMR-2308691). Hantong and Bi-Cheng acknowledge the funding support from NSF through the CAREER Grant DMR-2042284. Atom probe tomography was performed at the Northwestern University Center for Atom-Probe Tomography (NUCAPT, RRID: SCR_017770). NUCAPT received support from the MRSEC program (NSF DMR-2308691) at the Materials Research Center and the SHyNE Resource (NSF ECCS-2025633) at Northwestern University.

References

- [1] R. Manikandan, A. Raja Annamalai, Tungsten heavy alloys processing via microwave sintering, spark Plasma sintering, and additive manufacturing: A review, *Processes* 10 (2022) 2352.
- [2] A. Barua, S. Pradhan, M. Priyadarshini, A. Patra, K. Kumari, Recent advancement in tungsten heavy alloy processing for different industrial applications, *J. Mater. Eng. Perform.* 34 (2024) 8232-8252.
- [3] I. Singh, V.V. Dabholkar, Tungsten heavy alloys for kinetic energy penetrators: a review, *Mater. Sci. Technol.* 41 (2024) 235-256.
- [4] L. Lu, L. Zhu, L. Yuxiang, Corrosion performance of W-Ni-Cu and W-Ni-Fe alloys, *Rare Met. Mater. Eng.* 47 (2018) 1708-1715.
- [5] N.S. Shakunt, Gouthama, A. Upadhyaya, Effect of Fe addition in W-Ni-Cu heavy alloy processed through powder metallurgy on microstructure and mechanical properties, *J. Alloy. Compd.* 970 (2024) 172578.
- [6] S. S, A. Priyadarshini, P.K. Chaganti, G. Prabhu, P. Mylavaram, Effect of machining operations on mechanical properties, surface integrity and corrosion resistance of tungsten heavy alloy, *Mater. Today Commun.* 37 (2023).

- [7] N. Durlu, N.K. Çalışkan, Ş. Bor, Effect of swaging on microstructure and tensile properties of W–Ni–Fe alloys, *Int. J. Refract. Met. Hard Mater.* 42 (2014) 126–131.
- [8] D. Gu, Y. Li, H. Wang, Q. Jia, G. Zhang, Microstructural development and its mechanism of mechanical alloyed nanocrystalline W–10Ni alloy reinforced with Y_2O_3 nanoparticles, *Int. J. Refract. Met. Hard Mater.* 44 (2014) 113–122.
- [9] A. Kumari, M. Sankaranarayana, T.K. Nandy, On structure property correlation in high strength tungsten heavy alloys, *Int. J. Refract. Met. Hard Mater.* 67 (2017) 18–31.
- [10] U. Ravi Kiran, A. Panchal, M. Prem Kumar, M. Sankaranarayana, G.V.S. Nageswara Rao, T.K. Nandy, Refractory metal alloying: A new method for improving mechanical properties of tungsten heavy alloys, *J. Alloy. Compd.* 709 (2017) 609–619.
- [11] J. Das, G. Appa Rao, S.K. Pabi, M. Sankaranarayana, B. Sarma, Deformation behaviour of a newer tungsten heavy alloy, *Mater. Sci. Eng. A* 528 (2011) 6235–6247.
- [12] X. Gong, J. Fan, F. Ding, Tensile mechanical properties and fracture behavior of tungsten heavy alloys at 25–1100 °C, *Mater. Sci. Eng. A* 646 (2015) 315–321.
- [13] R.M. German, L.L. Bourguignon, B.H. Rabin, Microstructure limitations of high tungsten content heavy alloys, *JOM* 37 (1985) 36–39.
- [14] Y. Li, G.Q. Liu, X.B. Hu, L.H. Wu, C.W. Tan, V.P. Dravid, S.Z. Liu, A novel medium heavy alloy (MHA) with excellent static/dynamic properties and impact toughness, *Scripta Mater.* 162 (2019) 311–315.
- [15] Y. Li, Y. Xiong, J. Tang, S. Han, F. Ren, C. Wang, S. Wang, High-temperature tensile behavior of an as-cast Ni–W–Co–Ta medium–heavy alloy, *Coatings* 14 (2024) 323.
- [16] H. Wu, K. Wang, J. Duan, M. Li, X. Dai, G. Zhou, C. Wang, F. Zhao, Q. Zhang, Mechanical behaviors and microstructure evolution of Ni–W medium heavy alloy at various strain rates under uniaxial tension, *Int. J. Refract. Met. Hard Mater.* 117 (2023) 106399.
- [17] G. Cao, J. Dong, G. Xie, Z. Nie, T. Ma, B. Fu, A novel Ni–42W–10Co–1Mo medium–heavy alloy with excellent static/dynamic properties, *Adv. Eng. Mater.* (2025) 2402350.
- [18] S. Chen, T. Wang, X. Li, Y. Cheng, G. Zhang, H. Gao, Short-range ordering and its impact on thermodynamic property of high-entropy alloys, *Acta Mater.* 238 (2022).
- [19] J. Ding, Q. Yu, M. Asta, R.O. Ritchie, Tunable stacking fault energies by tailoring local chemical order in CrCoNi medium-entropy alloys, *Proc. Natl. Acad. Sci. U.S.A.* 115 (2018) 8919–8924.
- [20] R. Zhang, S. Zhao, J. Ding, Y. Chong, T. Jia, C. Ophus, M. Asta, R.O. Ritchie, A.M. Minor, Short-range order and its impact on the CrCoNi medium-entropy alloy, *Nature* 581 (2020) 283–287.
- [21] Z. Zhang, Z. Su, B. Zhang, Q. Yu, J. Ding, T. Shi, C. Lu, R.O. Ritchie, E. Ma, Effect of local chemical order on the irradiation-induced defect evolution in CrCoNi medium-entropy alloy, *Proc. Natl. Acad. Sci. U.S.A.* 120 (2023) e2218673120.
- [22] P. Cao, How does short-range order impact defect kinetics in irradiated multiprincipal element alloys?, *Acc. Mater. Res.* 2 (2021) 71–74.
- [23] M. Liu, A. Aiello, Y. Xie, K. Sieradzki, The effect of short-range order on passivation of Fe–Cr alloys, *J. Electrochem. Soc.* 165 (2018) C830–C834.
- [24] R. Zhang, S. Zhao, C. Ophus, Y. Deng, S.J. Vachhani, B. Ozdol, R. Traylor, K.C. Bustillo, J.W. Morris, D.C. Chrzan, M. Asta, A.M. Minor, Direct imaging of short-range order and its impact on deformation in Ti–6Al, *Sci. Adv.* 5 (2019) eaax2799.

[25] X. Zhou, H. Song, C. Guo, Z. Yang, F. Tian, Effect of short-range order on lattice distortion, stacking fault energy, and mechanical performance of Co-Fe-Ni-Ti high-entropy alloy at finite temperature, *Phys. Rev. Mater.* 8 (2024).

[26] D. Han, Y.J. Zhang, X.W. Li, A crucial impact of short-range ordering on the cyclic deformation and damage behavior of face-centered cubic alloys: A case study on Cu-Mn alloys, *Acta Mater.* 205 (2021) 116559.

[27] Z. Sun, C. Shi, C. Liu, H. Shi, J. Zhou, The effect of short-range order on mechanical properties of high entropy alloy $\text{Al}_{0.3}\text{CoCrFeNi}$, *Mater. Design* 223 (2022) 111214.

[28] G. Van Tendeloo, Short range order considerations and development of long range order in different Ni_4Mo alloys, *J. Phys. Chem. Solids* 35 (1974) 1317-1326.

[29] A. van de Walle, Multicomponent multisublattice alloys, nonconfigurational entropy and other additions to the Alloy Theoretic Automated Toolkit, *Calphad* 33 (2009) 266-278.

[30] A. van de Walle, M. Asta, G. Ceder, The alloy theoretic automated toolkit: A user guide, *Calphad* 26 (2002) 539-553.

[31] A.v.d. Walle, M. Asta, G. Ceder, Automating first-principles phase diagram calculations, *Journal of Phase Equilibria* 23 (2002) 348-359.

[32] H. Chen, S. Samanta, S. Zhu, H. Eckert, J. Schroers, S. Curtarolo, A. van de Walle, Bayesian active machine learning for Cluster expansion construction, *Comput. Mater. Sci.* 231 (2024).

[33] A. van de Walle, R. Sun, Q.-J. Hong, S. Kadkhodaei, Software tools for high-throughput CALPHAD from first-principles data, *Calphad* 58 (2017) 70-81.

[34] A. van de Walle, Invited paper: Reconciling SGTE and ab initio enthalpies of the elements, *Calphad* 60 (2018) 1-6.

[35] H. Chen, Q.-J. Hong, A. Navrotsky, A. van de Walle, A computational free energy reference for mechanically unstable phases, *Calphad* 91 (2025).

[36] G. Kresse, J. Hafner, Ab initio molecular dynamics for liquid metals, *Phys. Rev. B* 47 (1993) 558-561.

[37] G. Kresse, J. Furthmüller, Efficiency of ab-initio total energy calculations for metals and semiconductors using a plane-wave basis set, *Comput. Mater. Sci.* 6 (1996) 15-50.

[38] G. Kresse, J. Furthmüller, Efficient iterative schemes for ab initio total-energy calculations using a plane-wave basis set, *Phys. Rev. B* 54 (1996) 11169-11186.

[39] G. Kresse, D. Joubert, From ultrasoft pseudopotentials to the projector augmented-wave method, *Phys. Rev. B* 59 (1999) 1758-1775.

[40] P.E. Blochl, Projector augmented-wave method, *Phys. Rev. B* 50 (1994) 17953-17979.

[41] J.P. Perdew, K. Burke, M. Ernzerhof, Generalized gradient approximation made simple, *Phys. Rev. Lett.* 77 (1996) 3865-3868.

[42] F. Ducastelle, Order and phase stability in alloys, Elsevier Science1991.

[43] C.-L. Fu, R.P. Gorrey, B.-C. Zhou, A cluster-based computational thermodynamics framework with intrinsic chemical short-range order: Part I. Configurational contribution, *Acta Mater.* 277 (2024) 120138.

[44] Y. Rao, W.A. Curtin, Analytical models of short-range order in FCC and BCC alloys, *Acta Mater.* 226 (2022) 117621.

[45] P.R. Okamoto, G. Thomas, On short range order and micro-domains in the Ni_4Mo system, *Acta Metall.* 19 (1971) 825-841.

[46] N. Hansen, Hall–Petch relation and boundary strengthening, *Scripta Mater.* 51 (2004) 801-806.

[47] Z.C. Cordero, B.E. Knight, C.A. Schuh, Six decades of the Hall–Petch effect – a survey of grain-size strengthening studies on pure metals, *Int. Mater. Rev.* 61 (2016) 495-512.

[48] R.B. Figueiredo, M. Kawasaki, T.G. Langdon, Seventy years of Hall-Petch, ninety years of superplasticity and a generalized approach to the effect of grain size on flow stress, *Prog. Mater Sci.* 137 (2023) 101131.

[49] X. Li, W. Gao, Q. Jiang, Understanding the intrinsic framework of the Hall-Petch relationship of metals from the view of the electronic-structure level, *Acta Mater.* 292 (2025) 121071.

[50] T.J. Jang, Y.N. Lee, Y. Ikeda, F. Körmann, J.-H. Baek, H.-S. Do, Y.T. Choi, H. Gwon, J.-Y. Suh, H.S. Kim, B.-J. Lee, A. Zargaran, S.S. Sohn, Compositive role of refractory element Mo in improving strength and ductility of face-centered-cubic complex concentrated alloys, *Acta Mater.* 255 (2023) 119030.

[51] Z. Li, S. Ma, S. Zhao, W. Zhang, F. Peng, Q. Li, T. Yang, C.-Y. Wu, D. Wei, Y.-C. Chou, P.K. Liaw, Y. Gao, Z. Wu, Achieving superb strength in single-phase FCC alloys via maximizing volume misfit, *Mater. Today* 63 (2023) 108-119.

[52] G. Da Rosa, P. Maugis, A. Portavoce, J. Drillet, N. Valle, E. Lentzen, K. Hoummada, Grain-boundary segregation of boron in high-strength steel studied by nano-SIMS and atom probe tomography, *Acta Mater.* 182 (2020) 226-234.

[53] G.K. Williamson, R.E. Smallman, III. Dislocation densities in some annealed and cold-worked metals from measurements on the X-ray debye-scherrer spectrum, *Philos. Mag.* 1 (1956) 34-46.

[54] D. Kuhlmann-Wilsdorf, The theory of dislocation-based crystal plasticity, *Philos. Mag. A* 79 (1999) 955-1008.

[55] T. Ungár, A.D. Stoica, G. Tichy, X.-L. Wang, Orientation-dependent evolution of the dislocation density in grain populations with different crystallographic orientations relative to the tensile axis in a polycrystalline aggregate of stainless steel, *Acta Mater.* 66 (2014) 251-261.

[56] M. Walter, L. Mujica Roncery, S. Weber, L. Leich, W. Theisen, XRD measurement of stacking fault energy of Cr–Ni austenitic steels: influence of temperature and alloying elements, *J. Mater. Sci.* 55 (2020) 13424-13437.

[57] B.E. Warren, E.P. Warekois, Measurements of stacking faults in cold-worked alpha brass, *J. Appl. Phys.* 24 (1953) 951-952.

[58] J. Unfried-Silgado, L. Wu, F. Furlan Ferreira, C. Mario Garzón, A.J. Ramírez, Stacking fault energy measurements in solid solution strengthened Ni–Cr–Fe alloys using synchrotron radiation, *Mater. Sci. Eng. A* 558 (2012) 70-75.

[59] C.B. Li, Y. Zhang, Z.Q. Wang, D.Y. Shen, K.G. Wang, L.B. Liu, L.G. Zhang, Experimental investigation and thermodynamic re-assessment of the Fe–Ni–W phase diagram, *Calphad* 88 (2025) 102793.

[60] S. He, O.I. Gorbatov, P. Peng, First-principles-based statistical thermodynamic study of atomic interactions and phase stability in Ni-rich Ni–W alloys, *Calphad* 82 (2023) 102591.

[61] J. Popovič, P. Brož, J. Buršík, Microstructure and phase equilibria in the Ni–Al–W system, *Intermetallics* 16 (2008) 884-888.

Supporting Materials

Concentration-Dependent Tungsten Effects on Short-Range Order and Deformation Behavior in Ni–W alloys

Shaozun Liu^{1,7*}, Zehao Li², Hantong Chen³, Xingyuan San⁴, Bi-Cheng Zhou^{3*}, Dieter Isheim^{2,8},
Tiejun Wang¹, Hong Gao⁵, Nie Zhao⁶, Yu Liu¹, Yong Gan¹, Xiaobing Hu^{2,9*}

¹Central Iron and Steel Research Institute, Beijing 100081, China

²Department of Materials Science and Engineering, Northwestern University, Evanston, IL 60208,
USA

³Department of Materials Science and Engineering, University of Virginia, Charlottesville,
Virginia 22904, USA

⁴Hebei Key Lab of Optic-electronic Information and Materials, The College of Physics Science
and Technology, Hebei University, Baoding 071002, China

⁵Department of Physics, Beihang University, Beijing 100191, China

⁶School of Materials Science and Engineering, Xiangtan University, Xiangtan 411105, China

⁷Yangjiang Advanced Alloys Laboratory, Yangjiang 529500, China

⁸Northwestern University Center for Atom Probe Tomography (NUCAPT), Evanston, IL 60208,
USA

⁹The NUANCE Center, Northwestern University, Evanston, IL 60208, USA

*Corresponding authors. Email: xbhu@northwestern.edu (X.H.); liushaozun@cisri.com (S.L.);
bicheng.zhou@virginia.edu (B.C.Z.);

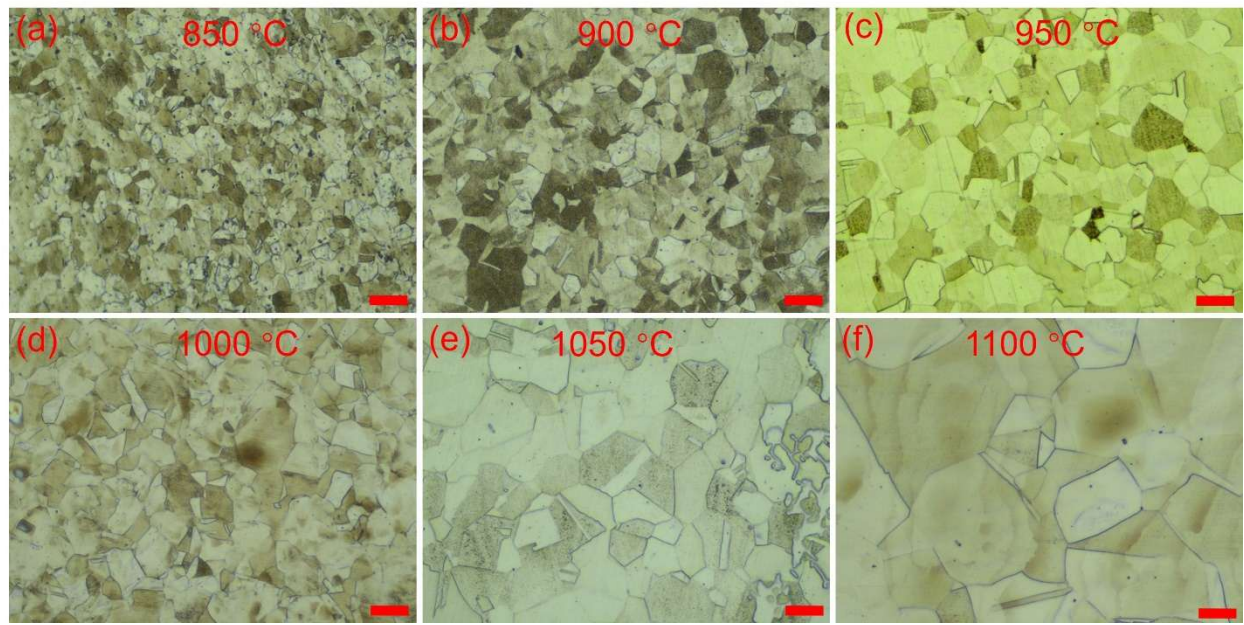


Figure S1. Optical micrograph of forged Ni-10W sample subjected to different solution temperatures. The scar bars in (a-f) are 50 μm .

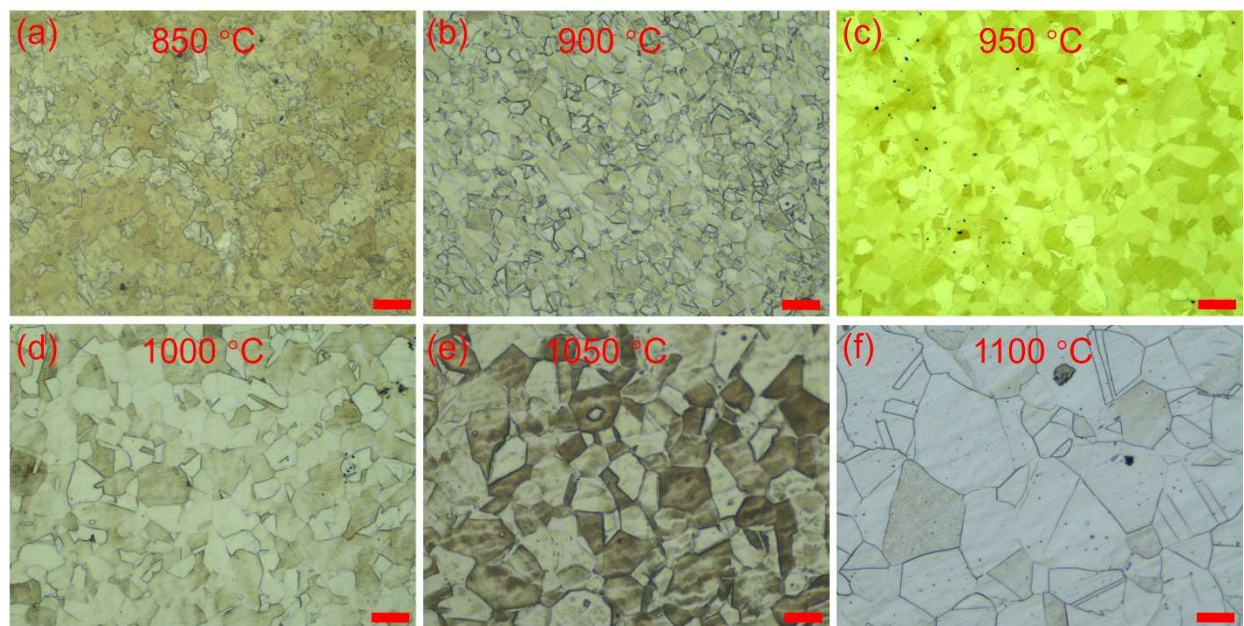


Figure S2. Optical micrograph of forged Ni-20W sample subjected to different solution temperatures. The scar bars in (a-f) are 50 μm .

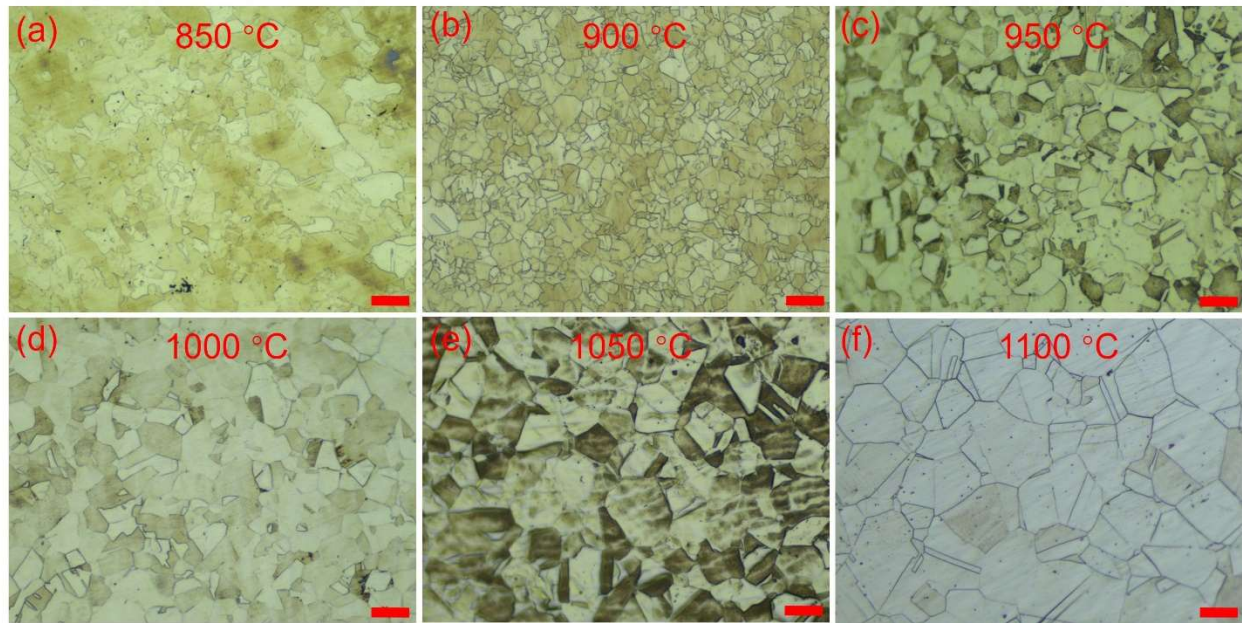


Figure S3. Optical micrograph of forged Ni-30W sample subjected to different solution temperatures. The scar bars in (a-f) are 50 μm .

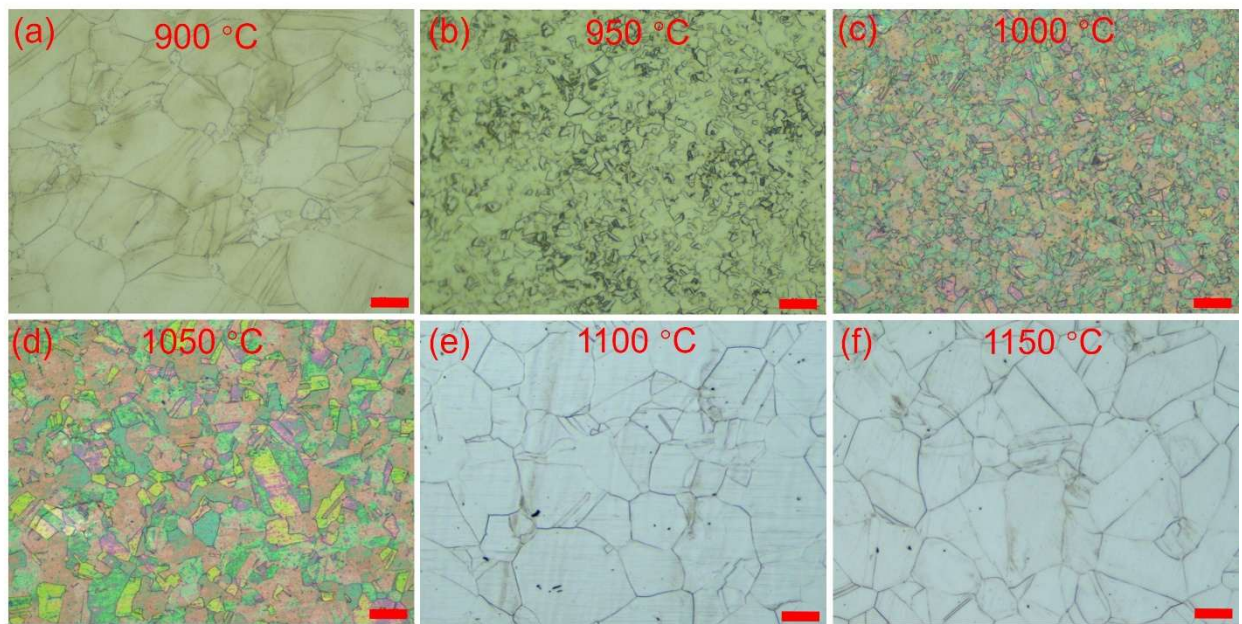


Figure S4. Optical micrograph of forged Ni-34W sample subjected to different solution temperatures. The scar bars in (a-f) are 50 μm . The abnormal microstructures in (a) indicates that the 900 °C is still not high enough to initiate the re-crystallization process for forged Ni-34W alloy.

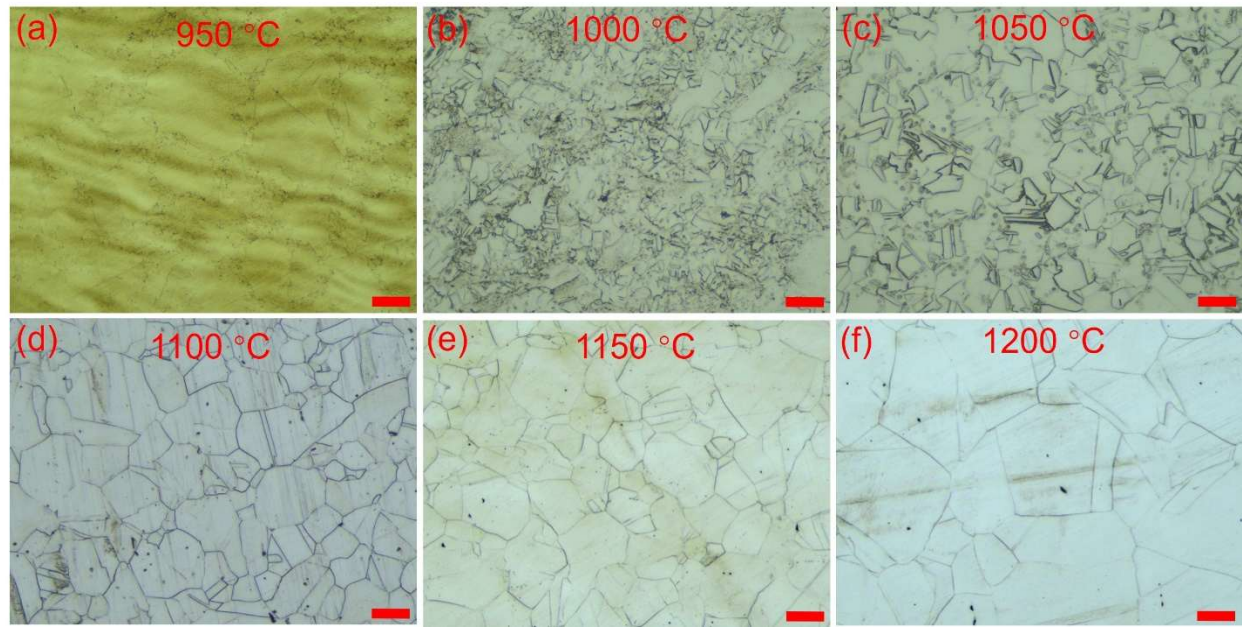


Figure S5. Optical micrograph of forged Ni-38W sample subjected to different solution temperatures. The scar bars in (a-f) are $50 \mu\text{m}$. The abnormal microstructures in (a) indicate that the $950 \text{ }^\circ\text{C}$ is still not high enough to initiate the re-crystallization process for forged Ni-38W alloy.

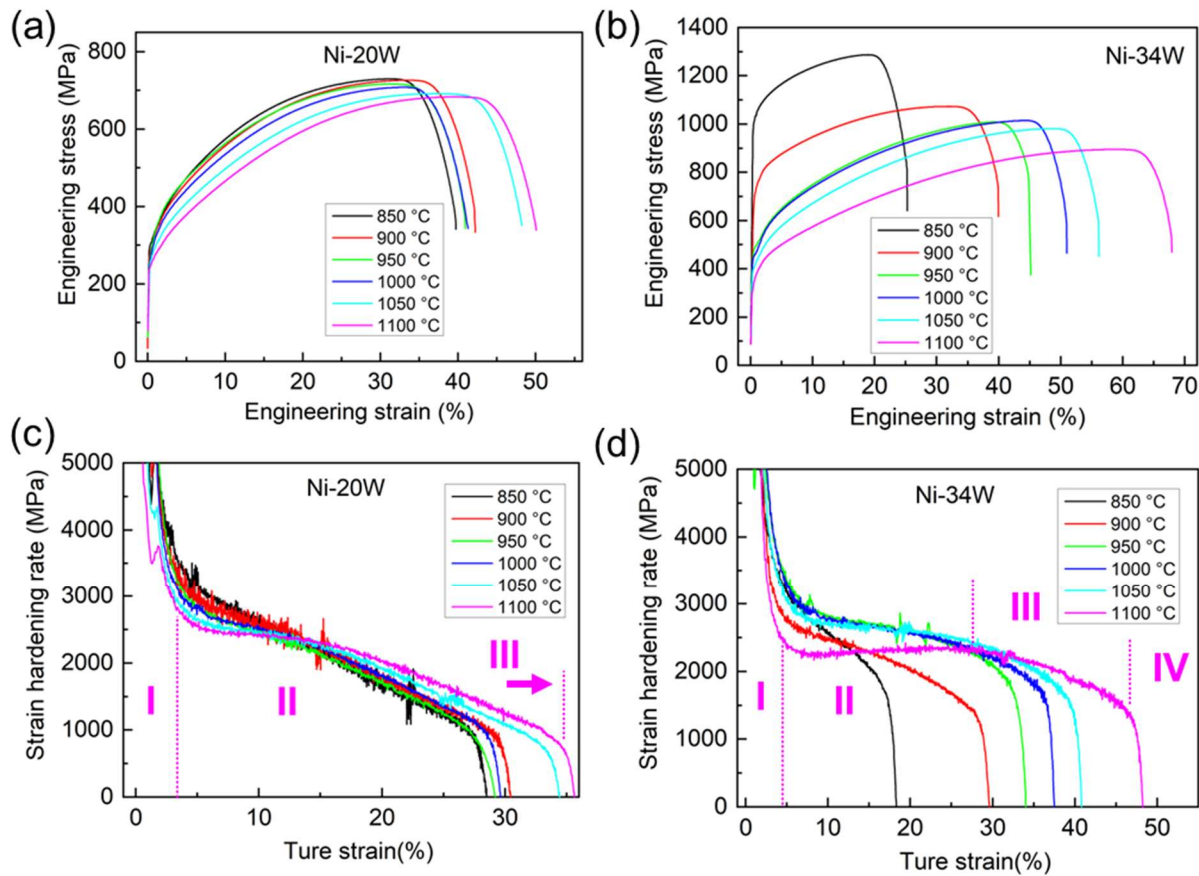


Figure S6. Engineering stress-strain and strain hardening rate curves of Ni-W binary alloys at different solution temperatures. (a, c) Ni-20W, (b, d) Ni-34W. The solution temperature for each curve is indicated in the legend. The vertical pink dash lines in (c) and (d) highlight the distinct deformation stages for Ni-20W solution-treated at 1100 °C, and Ni-34W solution-treated at 1100 °C respectively.

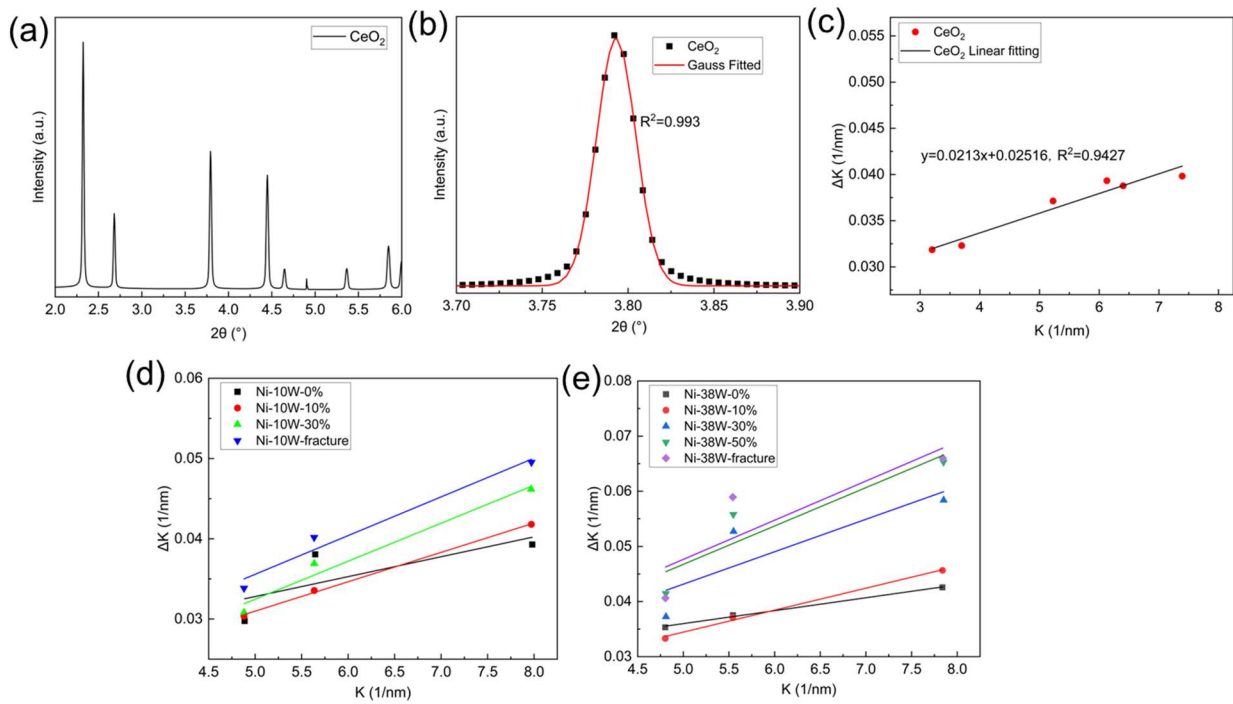


Figure S7. (a-c) Diffraction spectra, corresponding fitting results, and $K - \Delta K$ plots for CeO_2 . $K - \Delta K$ plots of (d) Ni-10W and (e) Ni-38W under various degrees of deformation. Ni-10W and Ni-38W are solution-treated at 1000 °C and 1100 °C, respectively.

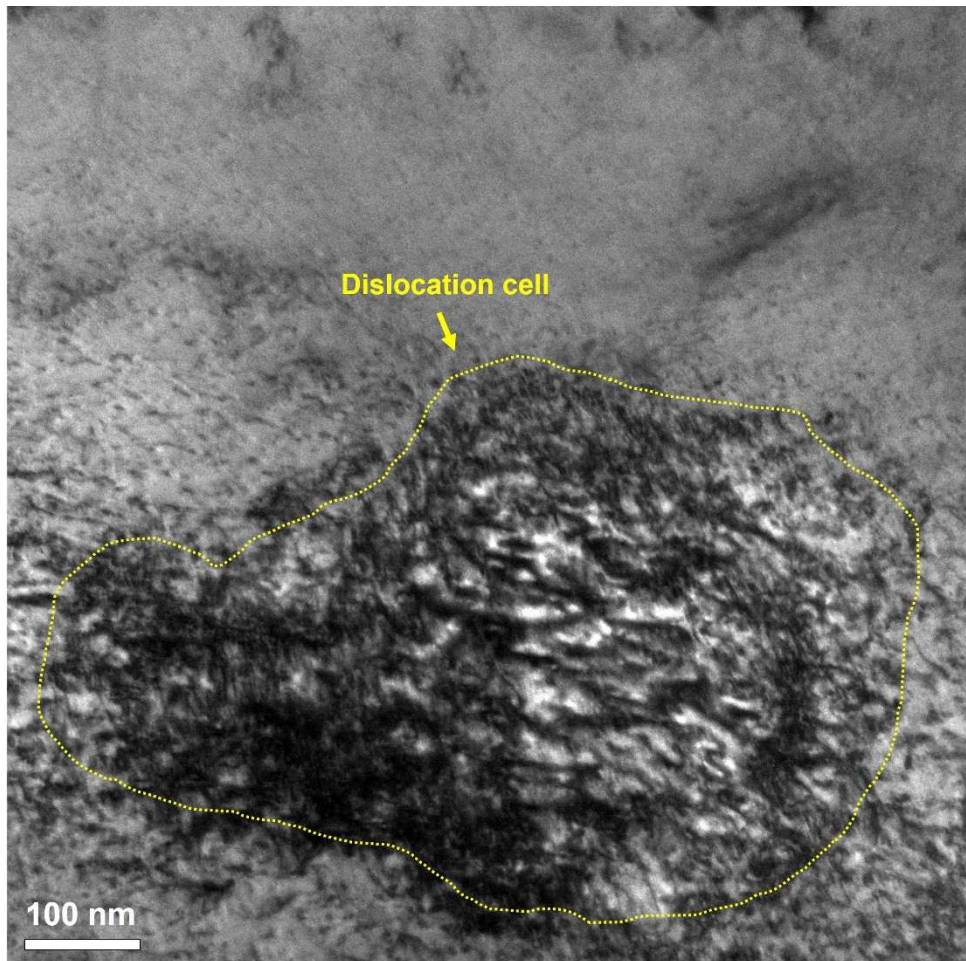


Figure S8. High magnification TEM image showing a typical dislocation cell structure within Ni-10W alloys (solution-treated at 1000 °C) deformed at 30%.

Table S1. Grain size (μm) of Ni-W binary alloys with varied W contents (wt.%) and solution temperatures (°C)

Solution temperature	Ni-10W	Ni-20W	Ni-30W	Ni-34W	Ni-38W
900	32	27	16	NA	NA
950	40	36	35	11	NA
1000	48	47	45	17	10.5
1050	65	58	55	32	36
1100	118	95	82	70	47
1150	NA	NA	NA	120	65
1200	NA	NA	NA	NA	140

Note: “NA” indicates “not applicable” for the specific alloys due to either too high or too low solution temperatures.

Table S2. Yield strength (MPa) of Ni-W binary alloys with varied W contents (wt.%) and solution temperatures (°C)

Solution temperature	Ni-10W	Ni-20W	Ni-30W	Ni-34W	Ni-38W
900	206	298	399	724	NA
950	201	289	354	485	1290
1000	198	279	336	458	593
1050	194	271	330	407	441
1100	181	253	299	339	414
1150	NA	NA	NA	318	388
1200	NA	NA	NA	NA	350

Note: “NA” indicates “not applicable” for the specific alloys due to either too high or too low solution temperatures.

Table S3. Ultimate tensile strength (MPa) of Ni-W binary alloys with varied W contents (wt.%) and solution temperatures (°C)

Solution temperature	Ni-10W	Ni-20W	Ni-30W	Ni-34W	Ni-38W
900	525	730	930	1077	NA
950	517	719	900	1009	1598
1000	514	710	854	1017	1146
1050	508	693	846	984	1026
1100	506	685	819	897	1015
1150	NA	NA	NA	827	938
1200	NA	NA	NA	NA	874

Note: “NA” indicates “not applicable” for the specific alloys due to either too high or too low solution temperatures.

Table S4. Elongation (%) of Ni-W binary alloys with varied W contents (wt.%) and solution temperatures (°C)

Solution temperature	Ni-10W	Ni-20W	Ni-30W	Ni-34W	Ni-38W
900	45	42	48.5	39.50	NA
950	45	40.5	52.5	44.5	20.0
1000	44	41	56	50.5	50.5
1050	42.5	48	58.5	55.5	53
1100	43.5	48	60	67	58
1150	NA	NA	NA	66	63
1200	NA	NA	NA	NA	66.5

Note: “NA” indicates “not applicable” for the specific alloys due to either too high or too low solution temperatures.

Note: Detailed procedure for SRO phase diagram generation

To start, cluster expansion was performed using the *mmaps* code in ATAT. The composition range was limited to 50 at% W, excluding the end member. The reference energy of FCC W was determined using the inflection detection method without lattice relaxation to account for its mechanical instability. The Bayesian fitting scheme was employed to obtain effective cluster interactions (ECIs) using the command:

```
mmaps -fa=bayesian
```

After obtaining the effective cluster interactions (ECI), the *phb* code was used to determine the phase boundary between Ni₄W and Ni. A representative command is:

```
phb -keV -er=15 -gs1=1 -gs2=2 -dx=1.0e-3 -T=100 -dT=25 -mu=-0.4
```

Here *-gs1=1* and *-gs2=2* specify the equilibrated phases listed in *gs_str.out*, and the chemical potential (*-mu*) should be adjusted to ensure correct phase boundary tracking.

The Monte Carlo simulation was performed using the *memc2* code to evaluate equilibrium configurations:

```
memc2 -keV -is=str.out -er=15 -n=100 -eq=500
```

Where *-is* denotes, the initial structure provides the starting composition for MC simulation. Additional parameters were defined in the *control.in* file.

The V-matrix, required to convert correlation functions into cluster probabilities, was generated using the *cvmclus* command:

```
cvmclus -d
```

To run *cvmclus*, a *maxclus.in* file is required. For calculating the SRO parameter for the first nearest neighbor, the *maxclus.in* file is just the smallest binary cluster. The code will generate the V matrix in *vmat.out* while also generating a *configmult.out* file. To obtain the SRO, we also need to extract the correlation matrix from the corresponding columns in the *mc.out* file generated through MC simulation by *memc2*. Then we need to multiply the correlation matrix with the V-matrix to obtain

the cluster probability. Finally, the cluster probability is multiplied with the multiplicity in *configmult.out* to obtain the true cluster probability.